communications earth & environment

Article

A Nature Portfolio journal

https://doi.org/10.1038/s43247-025-02719-x

Intraslab stress heterogeneity and continental mantle faulting revealed by the 2006 Pingtung offshore earthquake doublet

Wan-Lin Hu [1] ✉, Eh Tan [1], Ryo Okuwaki [2] ✉ & Yuji Yagi[2]

The impact of lithospheric rheology and subduction dynamics on intraslab stress and earthquake characteristics, as well as the cause of the scarcity of continental mantle earthquakes remain debated. We investigate the 2006 Pingtung offshore earthquake doublet (Mw 6.9) in the northern Manila subduction zone, where thinned continental lithosphere is subducting. These events exhibit complex source processes at mantle depths, making their fault geometry poorly constrained. Using potency density tensor inversion on teleseismic waveforms, we resolve the source process without predefined fault geometry. The first event exhibits normal faulting with minor reverse faulting at a deeper depth, while the second shows deeper strike-slip faulting. These diverse focal mechanisms reveal scattered mantle faulting and intraslab stress heterogeneity. Geodynamic modeling indicates mantle earthquakes require both strong subducting mantle lithosphere and substantial bending-induced differential stress. The global scarcity of such events stems from insufficient differential stress in most continental lithospheres.

Earthquakes within the continental mantle lithosphere are rare[1]. The reasons for their scarcity remain a topic of ongoing debate. A central question pertains to the strength of the continental lithospheric mantle. The strength of the continental mantle lithosphere is uncertain due to the complex compositional and thermal heterogeneities associated with the prolonged geological evolution of the continents. Some researchers attribute the rarity of mantle earthquakes to the weak rheology, i.e. ductility, of the continental mantle[1–3]. Others, however, argue that the mantle lithosphere is strong, but the tectonic stress is commonly insufficient to induce earthquakes[4,5]. Despite this, the sporadic occurrence of continental mantle earthquakes in some regions suggests that the mantle in those regions is strong enough to accumulate the elastic stress necessary for rupture[6]. Additionally, a strong mantle is proposed to be necessary to support the structural evolution of orogenic and subduction zones[4]. However, because continental mantle earthquakes are rare, resolving this debate remains difficult. The northern Manila subduction zone is notable for relatively frequent mantle lithosphere earthquakes[7–9] (Fig. 1), and represents a rare case where a thinned Eurasian continental crust and lithosphere is subducting under the Philippian Sea plate[10] (Fig. 1). The continental crust in this region is thinned, ranging from 10 to 30 km, due to its earlier tectonic history as the passive margin of the South China Sea[11–17]. In some areas, the crust is even thinner, with thicknesses less than 10 km[18]. Although the continental lithosphere in this region has undergone thinning, we assume it retains the compositional characteristics of typical continental lithosphere. Therefore, this region serves as a valuable natural laboratory for investigating the subduction of continental lithosphere and the findings from this study may have broader implications for understanding the behavior and strength of continental lithosphere in general.

Two major seismic events occurred at UTC 12:26 and 12:34 on December 26, 2006. These two events are an earthquake doublet, each with magnitudes of 7.1 and 6.9[19]. This doublet is referred to as the 2006 Pingtung offshore earthquake doublet[9,20], named after the coastal area in Taiwan. This doublet is not located on the subduction interface but within the subducting slab and composes intraslab events. Such events—like many intraslab earthquakes—are potentially more hazardous than typical interplate or crustal faulting events due to generally higher stress drops, greater radiated energy, and richer high-frequency content[21]. They, despite their potential to produce strong ground shaking, are often underrepresented in regional seismic hazard models[22]. These source characteristics, along with their

[1]Institute of Earth Sciences, Academia Sinica, Taipei, Taiwan. [2]Institute of Life and Environmental Sciences, University of Tsukuba, Tsukuba, Japan.
✉e-mail: huwanlin@earth.sinica.edu.tw; rokuwaki@geol.tsukuba.ac.jp

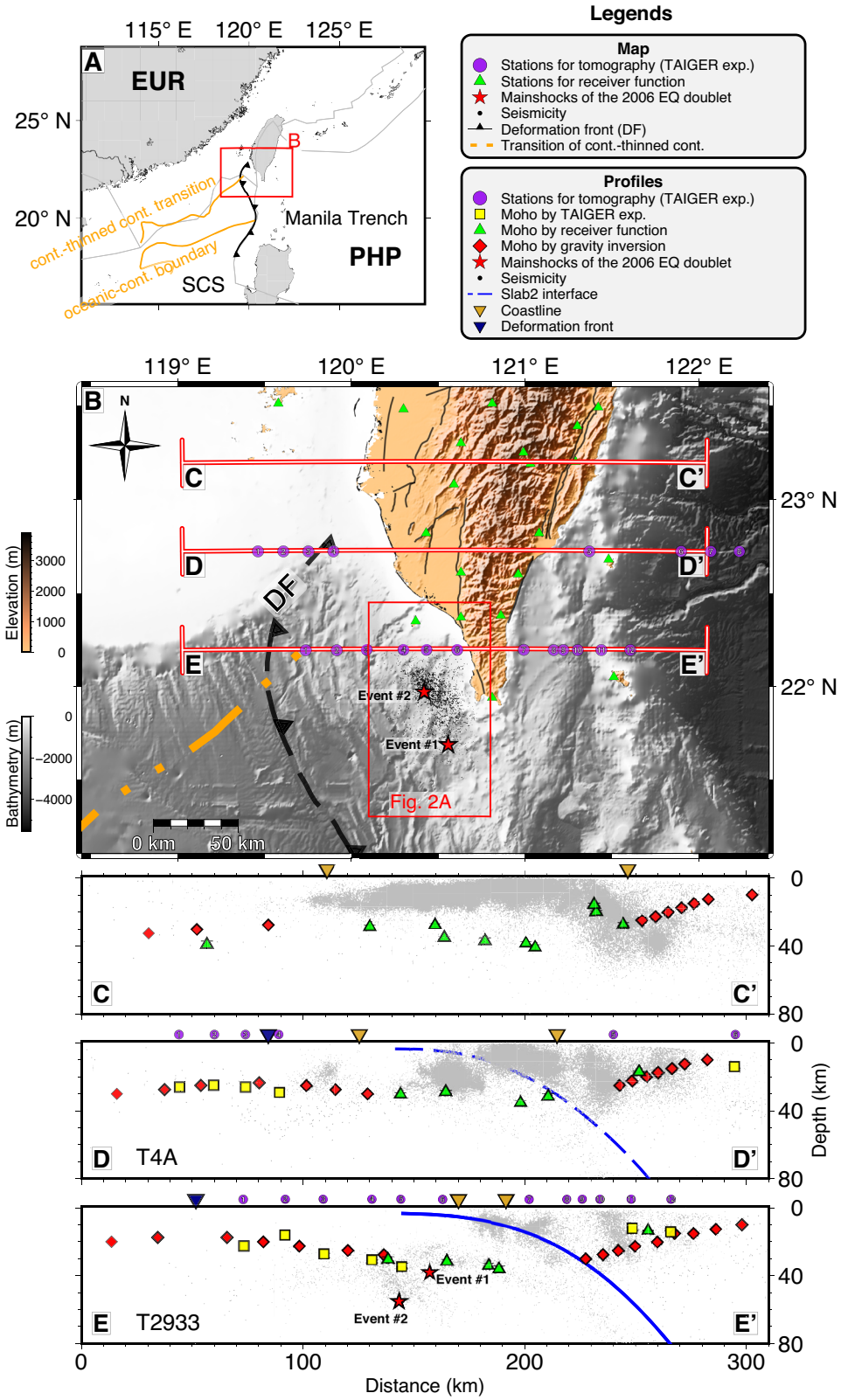

Fig. 1 | Regional maps and profiles illustrating geological features, seismicity, and variations in Moho depth. A displays a regional map. PHP refers to the Philippine Sea Plate, EUR represents the Eurasia Plate, and SCS denotes the South China Sea. The two orange lines mark key boundaries: the upper line indicates the continental-to-thinned continental transition, while the lower line marks the oceanic-to-continental boundary, as defined by Wang et al.[17]. The red box outlines the area shown in the (**B**). **B** illustrates the study area, including profiles' (**C**–**E**) locations, seismic stations, transition boundary between continental and thinned continental crust and deformation front (DF). The red box identifies the region depicted in Fig. 2 (**A**). On both the profiles (**C**-**E**) and the map (**B**), the locations of the 2006 Pingtung offshore earthquake doublet are indicated by red stars, determined by Central Weather Administration of Taiwan[25]. Slab interfaces from the Slab2 model[95] are shown as blue lines. The Moho depth from multiple studies are plotted: from the wide-angle seismic tomography (V_P = 7.8 km/s contour) by yellow squares[12,15,16], from gravity inversion by red diamonds[14], and from onshore receiver function by green triangles[13]. Relocated background seismicity from 1990 to 2020 and their depth uncertainties are plotted[9,96].

underlying physical controls, remain poorly understood, underscoring the need for deeper insight into intraslab rupture processes and their tectonic context. Due to poor station coverage, uncertainty in seismic velocity models, differences in analysis methods, and the complex rupture process, different studies report different depth estimates on this doublet (Table S1). However, a consistent pattern is observed across different catalogs, with the first event occurring at a shallower depth and the second event deeper (Table S1). The Global CMT[23] project lists the centroid depths at 19.6 km and 32.8 km for the two events, while the USGS catalog[19,24] places them at 25.5 km and 32.8 km, respectively. Relocated hypocenters from the Taiwan's Central Weather Administration[25] are 44.1 km and 50.2 km, respectively. Depth phase analysis indicates that the hypocenters and largest asperities of this doublet occurred at depths approximately 38 to 56 km, with the first event at a shallower depth than the second event[7]. A recent study[26]

combining regional data put the centroid depths at 28 and 44 km. In addition to their separated depths, this earthquake doublet exhibited distinct focal mechanisms. The first event displayed predominantly normal faulting, while the second, deeper event showed strike-slip faulting[19,23] (Fig. S1). This suggests considerable stress heterogeneity over a short vertical range. Additionally, the doublet's rupture processes, as evidenced by non-double couple components (Fig. S1)— ~15% and ~68%[24], respectively—should highlight the complexity of this event. Previous studies[7,20,26–28] have similarly indicated complex seismic source processes, but no consensus on a kinematic source model has been reached. Given the sensitivity of intraslab stress regimes on the lithospheric rheology[29] and subduction zone dynamics[30], constructing a comprehensive seismic source model could offer insights into the stress state and rheological parameters of the continental mantle lithosphere and the associated geodynamic implications.

In this study, we first explore seismic source characteristics by constructing a kinematic seismic source model, emphasizing on depth-dependent variations in source mechanisms. We then establish a viable geodynamic model of the seismic source area, whose stress regimes are consistent with that inferred from the constructed seismic source model. The results offer insights into regional lithospheric strength, providing explanations for the occurrence of mantle-depth earthquakes in this region, and aim to shed light on the broader question of why mantle earthquakes are rare in most continental lithospheres.

Due to the complex source processes and no fault geometry derived from surface expressions, developing a satisfactory source model for this doublet has been challenging. Previous studies of source characteristics have not reached a consensus[20,26,28], for the strikes and dips of the faults, and finite fault slip distributions for the doublet. To solve such complex source problem, most of the source studies would first have to construct a detailed fault model, inferred from near source surface displacement[31,32]. However, this doublet occurred offshore, and there is no observation on surface ruptures. In addition, this area has low background seismicity. Thus, we have no prior knowledge of the fault geometry. Since the Green's function is sensitive to the details of the assumed fault plane, the solution obtained would be highly dependent on the assumed fault plane[33]. An imprecise fault model can potentially compromise the accuracy of the seismic source solution and bias our interpretation. Another challenge is that although there are near-field strong motion stations[34], the events are outside the network area and have poor azimuthal coverage.

To address this issue, we apply an advanced finite-fault inversion method–Potency Density Tensor Inversion (PDTI)–which estimates the potency density tensor[35] projected onto the assumed model plane, as described in Shimizu et al.[36]. PDTI is a high-degree-of-freedom source inversion technique that uses teleseismic body waves, which offer broad azimuthal coverage and are relatively insensitive to the precise slip location. It represents slip direction on the model plane as a focal mechanism expressed by a linear combination of five basis double-couple components[37]. Importantly, PDTI allows estimation of the slip direction independently of the fixed orientation of the model plane[36]. This model domain can accommodate multiple faulting episodes of an event, without implying a single fault plane extending in a continuous rupture. The method estimates the spatiotemporal distribution of the potency-rate density tensor, including information on slip vectors and fault geometry or any focal mechanism required by the data, within the defined model domain. The strike of each model plane was determined based on focal mechanisms derived from the W-phase solutions in the USGS earthquake catalog[19,24]. For the first event (12:26 UTC), the model plane extends along a 171° strike, spanning a depth range of 10 to 60 km and a horizontal distance of 60 km, covering the potential depth range for the source processes. For the second event (12:34 UTC), the model plane strikes along 151° and spans a depth range from 20 to 70 km, extending 60 km along strike. Both strike directions are nearly parallel to the Manila Trench, likely reflecting structures associated with slab bending and unbending. For more details, see the Methods section #1.

We then set up 2D thermo-mechanical models focused on the seismic source region, oriented in the east–west direction, using elasto-visco-plastic rheology. Our 2D numerical code, geoflac, employs the Fast Lagrangian Analysis of Continua (FLAC) technique[38] for solving the conservation equations for mass and momentum and energy, the heat advection-diffusion equation with frictional heating. For details, see Method section #2. We setup the computational domain configured with dimensions of 1000 km in length and 300 km in depth, comprising 550 by 113 quadrilateral elements. The finest grid spacing, situated at the top center of the domain where the trench is located, is 1 km by 0.5 km. The initial model set up is shown in Fig. S2 and the parameters for initial model are shown in Table S3. The tectonic units, arranged from left to right, include the Eurasian continental shelf, continental slope, continent-ocean transition, South China Sea (SCS), and Philippine Sea Plate. The initial crustal thickness for each block is referenced from seismic reflection images at the northern SCS margin[17] and crossing the Hengchun Peninsula[39], where deformation is minimal, making these regions suitable proxies for the initial condition. A short slab of oceanic crust, approximately 6 km thick and 70 km long, is introduced into the mantle as a mechanical heterogeneity to facilitate subduction initiation. This configuration is a shortcut to achieve stable subduction quickly. A more realistic subduction initialization model would be proceeded by a slow and long convergence[40]. For boundary velocity, the Luzon Arc advances towards the Eurasian continent at a rate of 7–8 cm/yr along a 300°—310° azimuth[41]. The effective E-W convergence rate at the Manila Trench is approximately 5 cm/yr, which is equally partitioned between the two plates (i.e., 2.5 cm/yr each side) to maintain the trench at the center of the model and within the high-resolution region. Various convergence partitioning schemes tested in uniform-resolution models indicate that the partitioning does not notably impact the model outcomes[42]. The bottom boundary of the model is implemented as a Winkler foundation, allowing for both inflow and outflow, while the top boundary is a free surface incorporating hillslope diffusion to simulate surface process–erosion and sedimentation–controlled by a diffusivity coefficient (κ), which we set as 5×10^{-6} here. To consider the thermal structure for the geodynamic models in the seismic source area in the northern Manila subduction zone, we follow the temperature in the literature. Magnetic anomalies have been used to derive Curie temperature depths (~ 550 °C), suggesting that the Curie depth lies approximately 10 km beneath the Moho in the western offshore region of Taiwan[43]. A thermal structure model based on steady-state heat conduction, constrained by near-surface measurements of thermal conductivity and radiogenic heat production, further characterizes the regional thermal regime[44]. This model shows that the Moho temperature in the southern western offshore of Taiwan is about 500 °C. Additionally, a thermal model for the northern Manila Trench, constrained by heat flow observations, indicates that the temperature at the Moho is approximately 150–250 °C in the Philippine Sea Plate and 450–550 °C on the subducting thinned continental slab[45]. We explore several potential configurations of lithospheric rheology, which is not directly observable, and evaluate their predicted strain rates, stress regimes, accumulated plastic strain, and morphology to identify the model that best aligns with available observations. These observations include subduction zone morphology, Moho temperature, lithosphere-asthenosphere boundary (LAB) depth, crustal thickness, constrained by seismic tomographic images[12,16], as well as shear strain distributions inferred from seismic azimuth anisotropy[46].

Results and discussion

Kinematics of the earthquake source

The earthquakes in the 2006 Pingtung offshore doublet have similar magnitudes (Mw 6.9). Although their hypocenters are clearly separated, with the first event being shallower and the second event deeper, their depths reported by different studies vary (Table S1). To account for this uncertainty, we tested different initial rupture points within this range and identified the preferred model of the hypocenters, with the minimum variance in waveform fitting, at depths of 32.5 km for the first event and 47.5 km for the second event (Fig. S3). These depths are consistent with previously reported ranges[7,26] and align well with the depths of background seismicity (Fig. 2). Despite their proximity, the slip distributions of the

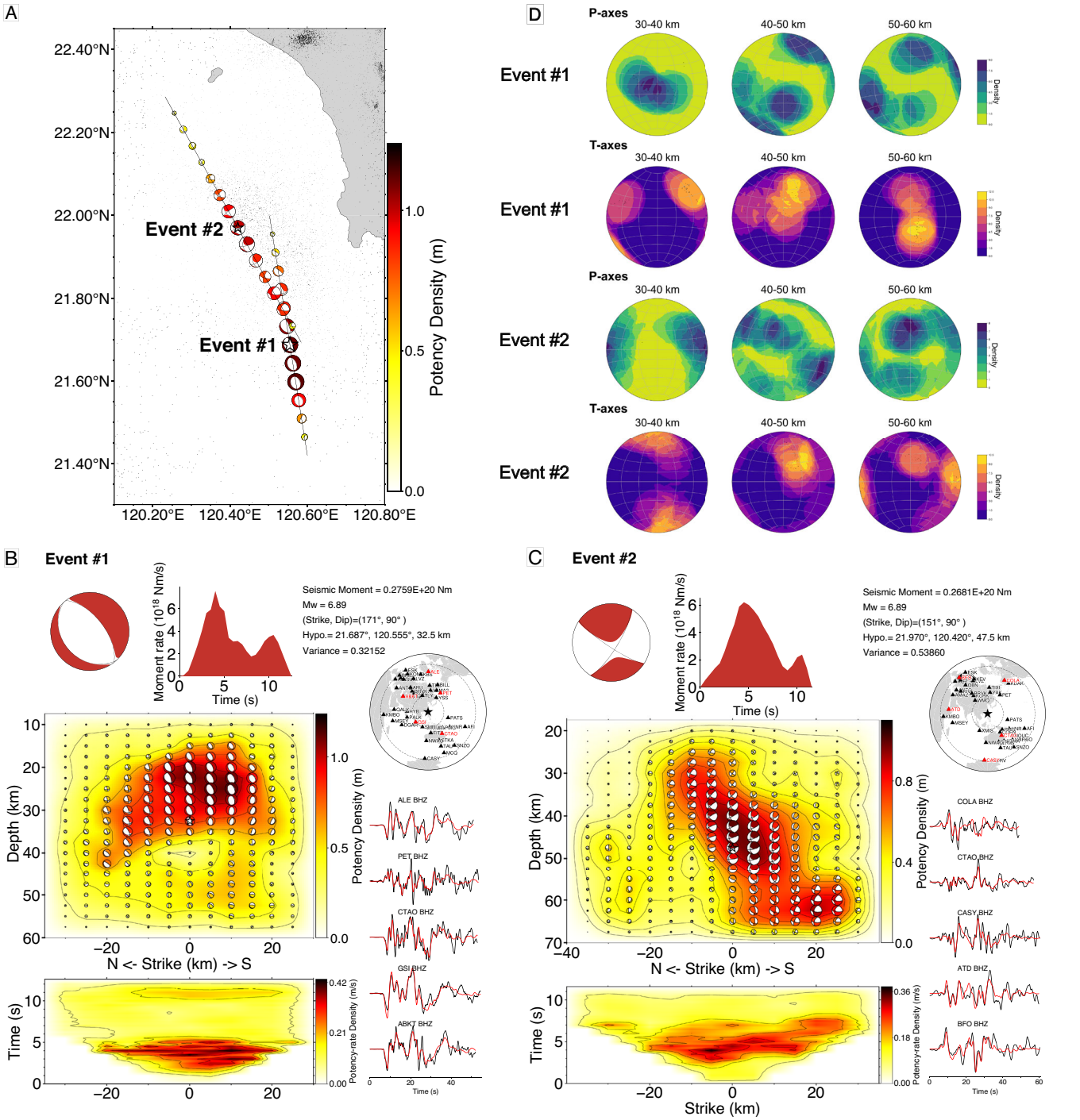

Fig. 2 | Seismic kinematic source models and P-, T-axes for the first event (26th Dec. 2006, UTC 12:26) and the second event (26th Dec. 2006, UTC 12:34) in the 2006 Pingtung offshore earthquake doublet. A Map view showing modeled spaces and focal mechanisms, with color and size scaled by potency-density. Black lines indicate surface traces of model planes for the first event and second event. **B**, **C** The panels include: (1) Map view showing the summed slip solution and focal mechanisms; (2) Moment rate functions for each event; (3) Slip distribution (potency density, in meters; see Methods section) on vertical model planes, with stars marking the initial rupture points. Focal mechanisms are shown in map view, and their projections onto the respective vertical planes are presented in cross-section view in Fig. S4. Depths are shown as absolute values (km); (4) Station distribution on the global map (triangles), with selected waveform fits shown for stations marked in red. Observed waveforms are plotted in black and synthesized waveforms in red. **D** Equal-angle stereonets illustrating P- and T-axes orientations, grouped in 10-km depth intervals, reveal depth-dependent variations in their orientations. For a comprehensive depth analysis, refer to Supplementary Fig. S14.

events exhibit distinct focal mechanisms at different depths, showing a combination of strike-slip, normal, and reverse faulting mechanisms.

For the first event, our preferred model with the rupture initiating at a depth of 32.5 km, providing the best waveform fit (Fig. S5). The rupture propagated both upward and downward, with the strike of the focal mechanisms and the azimuth and plunge of the P-axes varying systematically with depth (Fig. 2B and Figs. S6–8). This pattern aligns with Yen et al.'s[28] conclusion that the rupture occurred along discontinuous faults rather than a single, straight fault plane. Notable slip occurred primarily within the first 5 seconds (Fig. 2B), with the major rupture (or moment release) located at a shallower depth than the initial point. This may explain why centroid depth estimates[23,24] are typically shallower than hypocenter

depth estimates[25]. The shallower, predominant asperity shows normal faulting, with nearly vertical P-axes and horizontal T-axes, while the subsequent, minor asperity at greater depths transit to reverse faulting, with nearly horizontal P-axes and vertical T-axes (Fig. 2D), despite the relatively minor potency-rate density. While this previously unrecognized minor reverse component could potentially result from modeling artifacts, the transition persists in alternative models (Fig. S9) with various parameters, such as hypocenter depths. The overall focal mechanisms suggest layered faulting, with clear depth-dependent variations in the P- and T-axes, and near-simultaneous occurrence of normal and reverse faulting.

For the second event, the waveform fitting (Fig. S10) was generally poorer due to interference from the first event. The preferred model has the rupture initiating at a depth of approximately 47.5 km (Fig. 2C), further north and deeper than the first event, occurring ~474 s after the first event. The rupture propagated bidirectionally: upward towards the north and downward towards the south, primarily exhibiting a combination of strike-slip and reverse faulting mechanisms (Figs. S11–13). The P-axes exhibited varying azimuths but maintained predominantly low-angle plunges (~ 30°), consistently observed between ~20 km and 70 km depth (Fig. S14). Although the rupture episodes occurred in close spatial and temporal proximity, their fault geometries are distinctively different. The southern, deeper asperity rotated its strike by nearly 90° compared to the asperity near the hypocenter. This suggests that the events did not rupture the same fault but instead involved more distributed asperities, and that the later episodes may have been triggered by the initial one. An alternative model exhibits a similar rupture pattern, including the summed focal mechanisms and rupture downward (Fig. S15), reinforcing this observation. Notably, our summed focal mechanisms differ from those reported in the global catalogs such as USGS and GCMT (Fig. 2C), which use lower-frequency waveforms while the focal mechanism of the initial point closely matches those in the global catalogs (Fig. S1). This is likely because the global catalogs capture only the bulk source characteristics, whereas our broadband waveform analysis provides a more comprehensive view of the rupture process. In our solution, the initial point displays a pronounced non-double-couple component (Fig. 2C), suggesting multiple fault ruptures may have occurred at similar depths simultaneously. When present, high non-double-couple components in intraslab earthquakes have been linked to complex ruptures involving multiple fault planes[47,48].

The source models of this doublet indicate a change in P- and T- axes orientations with depth. In the next section, we will demonstrate that the depth-dependent stress orientation, consistent with the regional tectonics, explains our observation.

Geodynamic models

We now turn to geodynamic modeling to better understand a relationship between the seismic source and the tectonic setting. The model, shown in Fig. 3, represents the present-day configuration after 10 Myr of evolution, with 500 km of convergence—consistent with the estimates of subducted slab length[49]. We varied the strength of the continental crust and mantle in the models. We found that a relatively weak continental crust and strong mantle is required to reproduce the observed morphology of the Manila subduction zone (Fig. 3A). Such stratified lithospheric rheology is akin to the 'jelly sandwich' model and has been proposed in other regions[6].

First, we found that a stable subduction of continental lithosphere can be achieved only with a strong mantle lithosphere, where the brittle part of the lithospheric mantle is at least 20 km thick, as demonstrated in models with mantle strength stronger than model CM4 (Fig. S16). If the mantle were weaker, the strength of the subducting lithosphere will be too low so that it breaks continuously upon entering the trench (Fig. S16), as further detailed in Supplementary Text 1. Second, the morphology of the subduction zone, specifically the presence of accreted transitional crust[39,42], indicates weaker upper crustal layers decoupled from the mantle lithosphere. Otherwise, the transitional crust would simply subduct with the mantle lithosphere without accreting, as observed in other cases (Figs. S17, 18). Moreover, a weaker upper crust, decoupled from the lower crust, is indicated by the observed seismic azimuthal anisotropy[46], which points to a broad shear zone at ~20 km depth rather than a localized one (Fig. S18). The stress state in subducting plate with a 'jelly sandwich' rheology structure (preferred model: UC5_LC1_CM1) is characterized by horizontal compression and elastic bending. This combination creates high stress in the hinge zone of uppermost mantle lithosphere (Fig. 3E). This zone has a minor plastic strain up to 10^{-2} (Fig. 3D), indicating small amount of brittle failure, potentially manifesting as seismic events. Due to elastic bending, the high stress zone contains two layers. The upper layer, at approximately 30–40 km depth, is under extension with the first (the most compressive) principal stress (σ_1) oriented vertically and reaching values up to ~400 MPa (Fig. 3E). Below 40 km, the lower layer is under compression with a horizontal σ_1. Between the layers, a neutral stress plane develops where σ_1 diminishes and lacks a dominant orientation.

Depth-dependent stress heterogeneity revealed by the earthquake doublet

Our inversion of the first event in the doublet reveals a systematic transition in P- and T-axes with depth. In the shallower region (20–40 km), the P-axes are nearly vertical and the T-axes are horizontal. This pattern transitions at greater depths (40–60 km) to nearly horizontal P-axes and vertical T-axes (Fig. 2B, D, Fig. S6). Correspondingly, the inferred σ_1 orientation rotates from vertical to horizontal at approximately 40 km depth. This transition is similarly evident in the background seismicity, characterized by layered focal mechanisms (Fig. S19); although earthquakes at greater depths (> 50 km) are relatively infrequent, occasional strike-slip and reverse faulting events occur beneath a clustered layer of normal faulting (Fig. S19, profile W-E). The inversion of the deeper second event shows that both P- and T-axes maintain low-angle plunges across all depths while exhibiting azimuthal rotation with depth (Fig. 2C, D, Fig. S11). This indicates that σ_1 remain horizontal.

At comparable depths of ~50–60 km (Fig. 2B–D), the occurrence of strike-slip and reverse faulting suggests a predominantly horizontal σ_1, with permutations between the second (σ_2) and the third principal stresses (σ_3). These stress permutations may result from material heterogeneity[50] or lateral variations in slab buoyancy[51]. At depths of 20–40 km, the southern first event predominantly exhibits normal faulting, whereas the northern second event is characterized by strike-slip and reverse faulting (Fig. 2). This pattern aligns with the background seismicity: the southern segment, where the first event occurred, shows predominantly normal faulting, while the northern region, where the second event occurred, features strike-slip and reverse faulting at shallower depths (Fig. S19, profile N-S). These observations reveal longitudinal heterogeneity in the stress field.

Our 2D geodynamic model, while simplified for the spatial heterogeneity, effectively identifies the first-order stress regimes related to the long-term tectonic characteristics (Fig. 3E) and explains the observed seismic focal mechanisms and P-, T- axes (Fig. 2D, Figs. S6, S11). Validated against comprehensive observational constraints, the model reveals a notable rotation in σ_1 at approximately 40 km depth. This rotation results in a paired stress regime, characterized by shallower (updip) extension (normal faulting with vertical σ_1) and deeper (downdip) compression (reverse and strike-slip faulting with horizontal σ_1). This stress pattern, commonly attributed to slab bending, has been well-documented in intraslab regions of subduction zones[52,53]. Such a state of stress within intraslab is commonly indicated by the focal mechanisms of background seismicity, typically associated with mid-sized magnitude earthquakes[52,53]. When such stress regimes are observed through major events (Mw > 7 earthquakes), normal and reverse events across the neutral plane typically occur months or even years apart[54]. This temporal separation has led previous studies to suggest that the neutral plane might confine earthquake ruptures and limit their aftershock areas[55].

In our case, however, the first event of the doublet rupture propagated both updip and downdip, containing normal and reverse faulting styles. Next, the rupture of the second event, which propagated to deeper depths, predominantly exhibited strike-slip faulting. The ruptures propagated

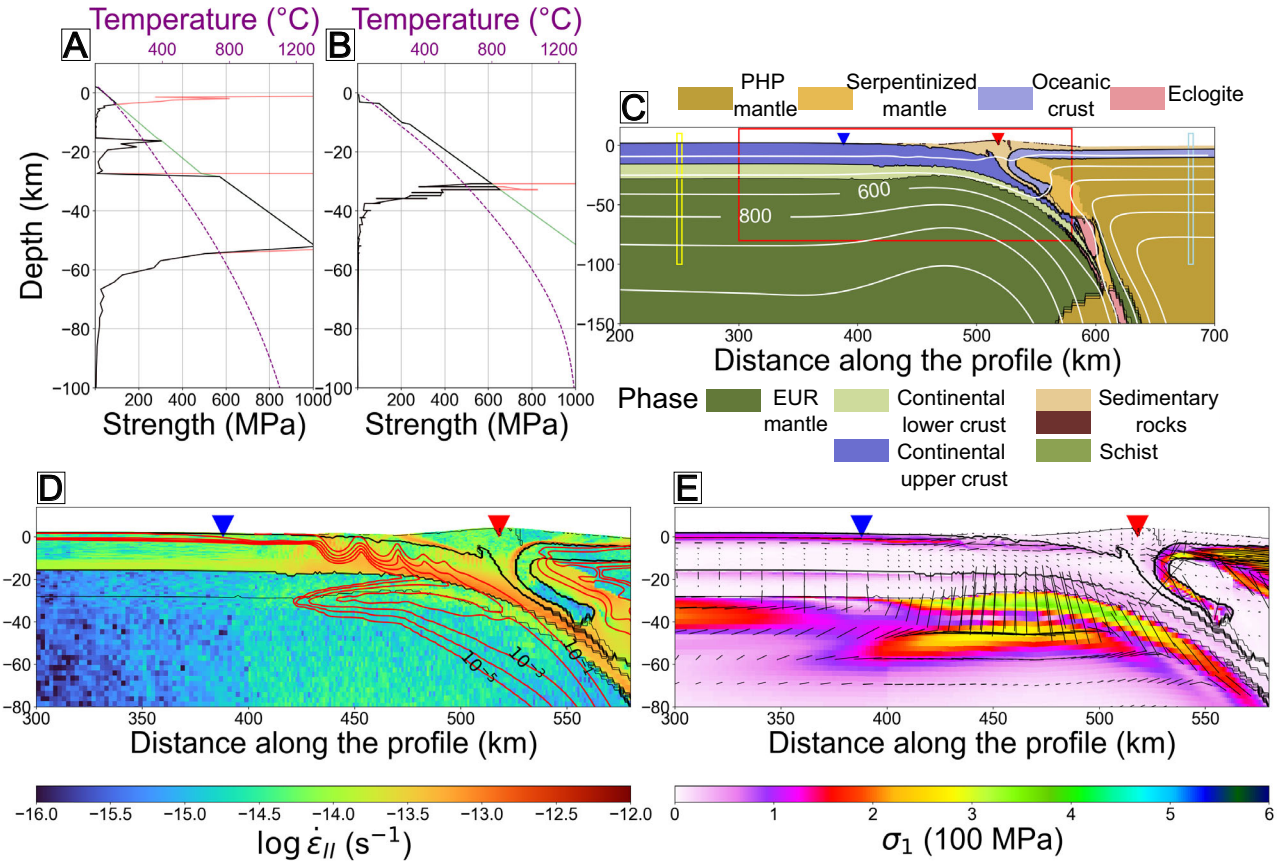

Fig. 3 | Geodynamic model in the northern Manila subduction zone. This figure presents our preferred geodynamic model at 2006's seismic source area. The procedure for acquiring the preferred model is detailed in the result section. **A** and **B** show the strength profiles for the Eurasian Plate (EUR) and Philippine Sea Plate (PHP), respectively, corresponding to the yellow and blue boxes in **C**. The red curve represents the viscous strength, which depends on the strain rate and temperature at that location; the green line indicates the frictional strength; the black line shows the lower of the two strengths, representing the lithospheric strength. The purple line denotes the temperature profile. **C** illustrates the phase distribution, illuminating the subduction zone morphology with white temperature contour with 200 °C intervals. **D** shows the second invariant of the deviatoric strain rate, with the red contours representing the plastic strain, ranging from 10^{-5} to 10^{-1}. **E** displays the orientation (short black bars) and magnitudes (in MPa) of the maximum principal stress (σ_1). **C**–**E** include black lines denote phase boundaries. The blue inverted triangles mark the deformation front, while the red inverted triangles indicate the accretionary wedge top.

through asperities separated by the inferred neutral plane, suggesting that the neutral plane may not serve as an effective barrier to rupture propagation. A similar case was observed in East Cape, New Zealand, at the southern end of the Kermadec Trench on March 4, 2021. The Mw 7.3 event started in the deeper part and was followed by shallower normal faulting[56], separated by approximately 20 s. The along-depth stress heterogeneity is revealed by focal mechanisms with opposite polarity occurring in close proximity in both time and space. Such phenomena might also exist in other subduction zones but have been overlooked or obscured in previous studies. Recent advancements in seismic source inversion techniques—such as the ability to solve for slip and focal mechanisms on unconstrained model planes with flexible fault geometries[36]—now allow for a more comprehensive capture of detailed rupture processes, including variations in focal mechanisms.

These observations of near-simultaneous rupture in reverse/strike-slip and normal focal mechanisms—which are intuitively conflicting and require dramatic stress rotation, are relatively rare. However, these findings reveal critical insights into rupture dynamics. For instance, opposing or diverse focal mechanisms can arise from permuted stress regimes due to along-strike variations in lithostatic loading[57] or from distinct stress regimes in subduction zones between the outer rise and inner trench[58]. These observations underscore the critical role of tectonic loaded stress in rupture complexity. This emphasizes the importance of considering the ambient and tectonic related stress environment in seismic source dynamic simulations to fully capture rupture scenarios.

Implications to lithospheric mantle rheology

Long-term lithospheric rheology is a critical factor controlling a variety of phenomena, including the surface topography, structural morphology, the evolution of tectonic features[5,59], and patterns in seismic distributions[60]. However, constraining lithospheric rheology, particularly that of the continental lithosphere, is challenging. Unlike the oceanic lithosphere, the continental lithosphere features a thick rheologically diverse, and stratified crust and mantle with properties that vary markedly across regions. This complexity arises from a complicate history involving variations in thermal history, fluid content, and composition, leading to ambiguities in understanding continental lithospheric rheology[61,62].

Lithospheric strength is commonly inferred from laboratory experiments[63]. However, extrapolating these laboratory results to long-term deformation remains debatable[5,63]. Lithospheric strength can also be inferred from seismicity distributions[64], though using earthquake occurrences—which are conditional and reflect transient mechanical instabilities—to gauge long-term lithospheric strength can be ambiguous[65]. Another option is to explore viable ranges of rheological parameters in numerical simulations of structural styles and morphology[4,59]. To ensure the long-term representativeness of our findings, in this study, we have not relied on any single dataset or observations confined to the same spatial-temporal scales. Instead, our study acquires rheological parameters from numerical experiments and drawing from observations across scales. These finding demonstrate that a long-term strong mantle is necessary not only for producing the observed intraslab stress heterogeneity within specific depth

ranges in the subduction zone, for maintaining stable subduction at the northern Manila subduction zone, but also for accumulating the elastic strain required to generate sub-Moho depth earthquakes up to Mw 6.9.

Why continental mantle earthquakes are rare?

Due to the rarity of mantle earthquakes under most continents, a generally weak mantle has been proposed for these regions[2]. Some researchers suggest that it is weakened by hydrous minerals[1] or an warm Moho, particularly above 600 °C[3]. Seismicity, being sensitive to thermal structure, is generally inferred to be restricted to the cooler regions of the slab above the neutral plane[66]. However, the fluid-content hypothesis does not adequately explain mantle earthquake distribution across diverse tectonic settings. Similarly, the temperature hypothesis, while influential, is not definitive. For example, the transition from stick-slip to stable sliding has been suggested to occur at temperatures as high as 800 °C[67], but this transition depends on a variety of factors. These factors include external variables such as strain rates, confining pressure condition, stress, and depth and intrinsic variables such as grain size, compositions, fluid contents, and deforming mechanisms[68]. Moreover, there are notable counterexamples that challenge the temperature hypothesis. For instance, some cold regions with theoretically favorable temperatures do not always exhibit seismic activity[69], while geological evidence suggests earthquakes can occur in regions with temperatures up to 720 °C[70]. Given this variability, temperature alone cannot fully explain the scarcity or occurrence of most of continental mantle earthquakes. Thus, broader and more general controlling factors must be considered.

Other researchers, primarily through numerical simulation approaches, suggest that a long-term strong lithospheric mantle is necessary to support the convergent stress induced from orogenesis and subduction[4,5]. If this is the case, and most of the brittle regime in continental mantle lithospheres does not experience earthquakes, the simplest explanation is a lack of sufficient differential stress. The Mohr-Coulomb yield stress increases by approximately 150 MPa for every 10 km of depth, assuming a density of 2600 kg/m^3 and a friction angle of 30°, making it more difficult to yield at the lower part of the brittle lithosphere. This suggests that brittle failure, and consequently mantle earthquakes, will be rare.

Our analysis indicates that the 2006 Pingtung offshore earthquake doublet occurred within a strong continental lithospheric mantle in the northern Manila subduction zone, where high bending stress imposed during subduction serves as a natural experiment to explore lithospheric strength. (Fig. 3E). In addition to bending-induced stress, the thinned continental crust in this region[16] results in a shallower mantle lithosphere compared to typical continental settings, reducing its yield strength. The combination of reduced strength and elevated bending stress creates a unique opportunity for yielding, manifested as plastic strain that collocates with enhanced stress in our geodynamic model (Fig. 3D) and with earthquake occurrence. Another line of evidence supporting the idea that the occurrence of mantle earthquakes follows stress availability is provided by Zhang et al.[51]. Their analysis of a slab flexure model shows that bending-induced stress reaches its peak in the northern Manila subduction zone, where seismicity is notably denser than in the southern segment. Moving further north toward the Taiwan orogeny, the degree of bending decreases[64,71], and the associated bending-induced stress is expected to weaken. This trend aligns with the observed reduction in mantle seismicity from profile E-E' to profile C-C' in Fig. 1. Profile C-C' represents a typical continental lithosphere, characterized by sparse lower crustal and mantle earthquakes.

Although the continental lithosphere in this study formed at a passive margin and has undergone thinning and stretching—conditions that may not characterize continental lithosphere in all tectonic settings—the conclusion regarding the critical role of sufficient tectonic stress appears to remain broadly applicable. Similar arguments have been made for cratonic regions, where tectonic stress well below the lithospheric strength is insufficient to cause yielding, resulting in infrequent seismic activity[72]. Supporting this argument, there are documented cases of earthquakes occurring within the continental mantle in regions where enhanced differential stress, driven by specific tectonic environments, creates conditions favorable for yielding. Examples include continental subduction in the northern Manila Trench, the Arafura Sea[73], and the Adriatic Sea[74], as well as continent–continent collision in the Tibet–Himalaya region[6,75].

Implications to seismic hazards of intraslab earthquakes

Concerning the source characteristics and hazard aspects of intraslab earthquakes, the 2006 Pingtung offshore earthquake doublet exemplifies how intraslab earthquakes may pose additional hazards by generating higher peak ground accelerations (PGA) than expected[76]. Detailed analysis of seismic source process in this study reveals that these intraslab earthquakes ruptured across multiple scattered and geometrically complex asperities. We propose that the geometric heterogeneity of these faults, characterized by small, discontinuous asperities, is indicative of an immature fault system. This is supported by minor plastic strain (10^{-3} to 10^{-1}) observed in the seismic source region of our geodynamic model (Fig. 3D). This behavior resembles that of crustal fault systems, where immature fault networks tend to exhibit greater fault misalignment[77]. Such misaligned or complex fault structures, coupled with heterogeneity in normal stress, can generate higher-frequency components in seismic waves–characteristics that may persist over multiple earthquake cycles, according to statistical analyses and experimental studies of crustal faults[78,79]. The observations and geodynamic modeling presented here offer a plausible explanation for the characteristically higher stress drops commonly observed in intraslab earthquakes[21]. The higher stress drop is likely a consequence of misaligned, immature fault networks, as subducting slabs experience concentrated stress only in limited zones and lack the consistent stress loading necessary for fault maturation over time, unlike interplate fault systems.

Methods

#1 potency density tensor inversion method

A potency-density tensor inversion method[36] was proposed to flexibly accommodate multiple faults with complex geometries rupturing during the same event. In the flexible source inversion method, fault slip along the assumed model plane is represented by the superposition of five basis double-couple components[37]; then, the fault geometry can be inferred from the spatiotemporal variation of focal mechanisms. This method mitigates the effect due to the uncertainty of the fault geometry by obtaining the distribution of potency-rate density tensors (i.e., spatiotemporal distribution of slip and the fault geometry)[35,37] along the assumed model plane.

In the PDTI method, the seismic waveform u_j observed at a station j is expressed as follows:

$$u_j(t) = \sum_{q=1}^{5} \int_S \left(G_{qj}(t,\xi) + \delta G_{qj}(t,\xi) \right) * \dot{D}_q(t,\xi) d\xi + e_{bj}(t) \quad (1)$$

where G_{qj} is the Green's function of the q-th component of the double-couple moment tensor, δG_{qj} is the modeling error on G_{qj}[80], $\dot{D}_q$ is the potency-rate density function, e_{bj} is a background and instrumental Gaussian noise, ξ represents a position on the assumed model plane (S), and $*$ denotes the convolution operator in the time domain t. A potency density tensor is obtained by dividing a moment density tensor by rigidity of the medium. The PDTI projects the faulting slip on the model plane as potency density tensors, which relates to the slip if the projected plane is a true fault plane[36].

To avoid overfitting and unstableness that may arise from such a high-degree of freedom modeling, the PDTI explicitly introduces modeling errors originated from the uncertainty of the Green's function into the data covariance matrix[80] and adopts Akaike's Bayesian Information Criterion (ABIC)[81–84] to objectively determine the strength of smoothing constraints. We followed the latest time-adaptive method that dynamically adjusts the smoothing strength based on the amplitude of the potency-rate density function. This approach effectively reduces over-smoothing during the main rupture, preserving the clarity of the results[85]. The Green's function

was computed based on the method of Kikuchi & Kanamori[37] using a one-dimensional velocity structure[16] for the source side (Table S1). To mitigate the effects of the Earth's three-dimensional velocity structure, P-wave arrival times were manually picked.

This method has effectively resolved cases involving complex rupture processes with undefined fault geometry across various tectonic settings, as demonstrated in recent studies[47,56,86–89]. When compared with results from cases like the Kaikoura earthquake in 2016[31,90] and the El Mayor-Cucapah earthquake in 2010[32,85], where the fault traces can be defined from the surface, this method consistently shows stability and reproducibility in addressing source problems, particularly in determining focal mechanisms that indicate stress states. Moreover, it reveals distinct advantages in regions lacking known faults, addressing unique challenges that are otherwise intractable, such as intraslab earthquake in East Cape, New Zealand[56].

Model configurations

We set the strike of our modeled planes for both events according to the USGS's moment tensor solutions. In the PDTI, the potency density tensor at each node is solved independently of the model plane. For both events, spatial node intervals are 2.5 km along depth and 5 km along strike, resulting in a total of 240 source elements (subfaults) (Fig. 2A–C). We adopt the hypocenter at 21.687°N, 120.555°E, 32.5 km and 21.970°N, 120.420°E, 47.5 km, for the first and the second event, respectively. The location (latitude, longitude) is determined by CWB relocation. The maximum rupture-front velocity was limited to 4.4 km/s. The potency-rate density function for each spatial node was assumed to be a linear B-spline function with 0.5 s intervals, with a total duration of 12 s and 11 s for the first and second event, respectively. The sensitivity of the model-plane geometry and the near-source structural models is evaluated, which turns out to have limited effect on the solution (Figs. S20, S21).

#2 Geodynamic (thermal-mechanical) models

Our 2D numerical code, geoflac, employs the Fast Lagrangian Analysis of Continua (FLAC) technique[38] for solving the conservation equations for mass and momentum and energy, the heat advection-diffusion equation with frictional heating. The detailed algorithm, described by previous studies[91–93], is briefly summarized here. The equation of motion is solved explicitly on a Lagrangian grid with strong damping (5e-5) of the elastic wave to achieve quasi-static equilibrium.

Equations and parameters governing mechanical behavior

The model's mechanical behavior is governed by elasto-visco-plastic constitutive relationship. Linear elasticity is computed using the Lamé first (λ_1) and second parameters (λ_2), 3×10^{10} Pa here. For plasticity, the shear stress at yield τ, follow the Mohr-Coulomb yield criterion ($\tau = \sigma_n \tan(\phi) + C$), depends on normal stress (σ_n), cohesion (C) and friction angle (ϕ). Cohesion and friction angle decrease linearly with plastic strain from initial (C_0, ϕ_0) to weakened values (C_1, ϕ_1) until the plastic strain reaches the saturated plastic strain, which is assigned a value of 0.1 in our model. The values for density, cohesion and friction of different materials are listed in Table S3. In all models, except the serpentinized mantle and sediments, all other lithospheric materials weaken frictionally from $\phi = 30°$ to $\phi = 15°$.

Viscosity η is nonlinear, depending on the deviatoric strain rate's second invariant ($\dot{\varepsilon}_{II} = 1/2\sqrt{\left(\dot{\varepsilon}_{xx} - \dot{\varepsilon}_{zz}\right)^2 + 4\dot{\varepsilon}_{xz}^2}$), stress exponent (n), viscosity pre-factor (A), activation energy (E), universal gas constant (R), and temperature (T) and is calculated using the non-Newtonian dislocation creep law as follows[94]:

$$\eta = \frac{1}{4}\left(\frac{3}{4A}\right)^{\frac{1}{n}} \dot{\varepsilon}_{II}^{\frac{1-n}{n}} exp\left(\frac{E}{nR(T+273)}\right) \quad (2)$$

Despite viscosity reduction with temperature and strain, a minimum cut-off value of 10^{20} Pa·s is imposed. Stresses from elasto-viscous and elasto-plastic flow are computed for each element, with the lesser stress invariant taken as the final stress.

Data availability

All seismic data were downloaded through the IRIS Wilber 3 system (https://ds.iris.edu/wilber3/). The facilities of EarthScope Consortium were used for access to waveforms and related metadata from the following seismic networks: (a) the BK (BDSN; Northern California Earthquake Data Center, 2014); (b) the G (GEOSCOPE; Institut De Physique Du Globe De Paris (IPGP) & Ecole Et Observatoire Des Sciences De La Terre De Strasbourg (EOST), 1982); (c) the GE (GEOFON; GEOFON Data Center, 1993); (d) the IC (NCDSN; Albuquerque Seismological Laboratory (ASL)/USGS, 1992); (e) the IU (GSN–IRIS/USGS; Albuquerque Seismological Laboratory/USGS, 2014); (f) the MN (MedNet; MedNet Project Partner Institutions, 1990); and (g) the PS (ERI/STA; University of Tokyo, Earthquake Research Institute (Todai, ERI), Japan, 1989). Additional datasets include the Geophysical Database Management System (GDMS) in the Central Weather Administration (DOI: 10.7914/SN/T5), centroid moment tensor solutions from the GCMT catalog (https://www.globalcmt.org/CMTsearch.html), the USGS catalog, TECDC (DOI: 10.30067/TECNL.202206_1(1).0002), and the AutoBATS CMT catalog (https://tecdc.earth.sinica.edu.tw/FM/AutoBATS/). Data from Y. M. Wu et al. (2009, 2013) were obtained from http://seismology.gl.ntu.edu.tw/main.htm.

Code availability

The code for 2D geodynamic modeling is available at https://github.com/GEOFLAC/geoflac.

Received: 31 March 2025; Accepted: 19 August 2025;
Published online: 30 August 2025

References

1. Maggi, A., Jackson, J. A., McKenzie, D. & Priestley, K. Earthquake focal depths, effective elastic thickness, and the strength of the continental lithosphere. *Geology* **28**, 495–498 (2000).
2. Jackson, J. Strength of the continental lithosphere: Time to abandon the jelly sandwich?. *GSA Today* **12**, 4 (2002).
3. Jackson, J., McKenzie, D. & Priestley, K. Relations between earthquake distributions, geological history, tectonics and rheology on the continents. *Philos. Trans. R. Soc. Math. Phys. Eng. Sci.* **379**, 20190412 (2021).
4. Burov, E. B. & Watts, A. B. The long-term strength of continental lithosphere: "jelly sandwich" or "crème brûlée"?. *GSA Today* **16**, 4 (2006).
5. Burov, E. B. Rheology and strength of the lithosphere. *Mar. Pet. Geol.* **28**, 1402–1443 (2011).
6. Chen, W.-P. & Molnar, P. Focal depths of intracontinental and intraplate earthquakes and their implications for the thermal and mechanical properties of the lithosphere. *J. Geophys. Res. Solid Earth* **88**, 4183–4214 (1983).
7. Chen, Y. R., Lai, Y. C., Huang, Y. L., Huang, B. S. & Wen, K. L. Investigation of source depths of the 2006 Pingtung earthquake sequence using a dense array at teleseismic distances. *Terr. Atmos. Ocean. Sci.* **19**, 579–588 (2008).
8. Lin, C.-H. Compelling evidence of an aseismic slab beneath central Taiwan from a dense linear seismic array. *Tectonophysics* **466**, 205–212 (2009).
9. Wu, Y. M. et al. Relocation of the 2006 Pingtung Earthquake sequence and seismotectonics in Southern Taiwan. *Tectonophysics* **479**, 19–27 (2009).
10. Taylor, B. & Hayes, D. E. Origin and History of the South China Sea Basin. in *The Tectonic and Geologic Evolution of Southeast Asian Seas and Islands: Part 2* 23–56 https://doi.org/10.1029/GM027p0023. (1983).
11. Chen, M., Fang, J. & Cui, R. Lithospheric structure of the South China Sea and adjacent regions: Results from potential field modelling. *Tectonophysics* **726**, 62–72 (2018).

12. Eakin, D. H. et al. Crustal-scale seismic profiles across the Manila subduction zone: The transition from intraoceanic subduction to incipient collision. *J. Geophys. Res. Solid Earth* **119**, 1–17 (2014).
13. Goyal, A. & Hung, S. H. Lateral Variations of Moho Depth and Average Crustal Properties Across the Taiwan Orogen From H-V Stacking of P and S Receiver Functions. *Geochem. Geophys. Geosyst.* **22**, 1–26 (2021).
14. Gozzard, S. et al. South China sea crustal thickness and oceanic lithosphere distribution from satellite gravity inversion. *Pet. Geosci.* **25**, 112–128 (2019).
15. Lester, R. et al. Crustal accretion in the Manila trench accretionary wedge at the transition from subduction to mountain-building in Taiwan. *Earth Planet. Sci. Lett.* **375**, 430–440 (2013).
16. McIntosh, K. et al. Inversion of a hyper-extended rifted margin in the southern Central Range of Taiwan. *Geology* **41**, 871–874 (2013).
17. Wang, T. K., Chen, M. K., Lee, C. S. & Xia, K. Seismic imaging of the transitional crust across the northeastern margin of the South China Sea. *Tectonophysics* **412**, 237–254 (2006).
18. Rodrigues De Vargas, M., Tugend, J., Mohn, G., Kusznir, N. & Liang-Fu, L. Crustal structure of the Northeast South China sea rifted margin. *Tectonics* **43**, e2024TC008399 (2024).
19. U.S. Geological Survey, Earthquake Hazards Program. Advanced National Seismic System (ANSS) Comprehensive Catalog of Earthquake Events and Products: Various. https://doi.org/10.5066/F7MS3QZH. (2017).
20. Lee, S. J., Liang, W. T. & Huang, B. S. Source mechanisms and rupture processes of the 26 December 2006 Pingtung earthquake doublet as determined from the regional seismic records. *Terr. Atmos. Ocean. Sci.* **19**, 555–565 (2008).
21. Ye, L., Lay, T. & Kanamori, H. Large earthquake rupture process variations on the Middle America megathrust. *Earth Planet. Sci. Lett.* **381**, 147–155 (2013).
22. Kikuchi, M. & Kanamori, H. The Shikotan Earthquake of October 4, 1994: Lithospheric earthquake. *Geophys. Res. Lett.* **22**, 1025–1028 (1995).
23. Ekström, G., Nettles, M. & Dziewoński, A. M. The global CMT project 2004–2010: Centroid-moment tensors for 13,017 earthquakes. *Phys. Earth Planet. Inter.* **200–201**, 1–9 (2012).
24. Duputel, Z., Rivera, L., Fukahata, Y. & Kanamori, H. Uncertainty estimations for seismic source inversions. *Geophys. J. Int.* **190**, 1243–1256 (2012).
25. Central Weather Administration (CWA, Taiwan) Central Weather Administration Seismographic Network. *Int. Fed. Digital Seismogr. Netw.* https://doi.org/10.7914/SN/T5 (2012).
26. Hu, G. et al. Source characteristics of the 2006 Pingtung earthquake doublet off southern Taiwan and the possible contribution of submarine landslides to the Tsunami. *Earth Planet. Sci. Lett.* **643**, 118921 (2024).
27. Huang, B. S., Huang, Y. L., Lee, S. J., Chen, Y. G. & Jiang, J. S. Initial rupture processes of the 2006 Pingtung earthquake from near source strong-motion records. *Terr. Atmos. Ocean. Sci.* **19**, 547–554 (2008).
28. Yen, Y. T., Ma, K. F. & Wen, Y. Y. Slip partition of the 26 December 2006 Pingtung, Taiwan (M 6.9, M 6.8) earthquake doublet determined from teleseismic waveforms. *Terr. Atmos. Ocean. Sci.* **19**, 567–578 (2008).
29. Kaus, B. J. P., Liu, Y., Becker, T. W., Yuen, D. A. & Shi, Y. Lithospheric stress-states predicted from long-term tectonic models: Influence of rheology and possible application to Taiwan. *J. Asian Earth Sci.* **36**, 119–134 (2009).
30. Carminati, E. & Petricca, P. State of stress in slabs as a function of large-scale plate kinematics. *Geochem. Geophys. Geosyst.* **11**, 2009GC003003 (2010).
31. Hamling, I. J. et al. Complex multifault rupture during the 2016 M_w 7.8 Kaikōura earthquake, New Zealand. *Science* **356**, eaam7194 (2017).
32. Wei, S. et al. Superficial simplicity of the 2010 El Mayor–Cucapah earthquake of Baja California in Mexico. *Nat. Geosci.* **4**, 615–618 (2011).
33. Yagi, Y., Mikumo, T., Pacheco, J. & Reyes, G. Source rupture process of the Tecomán, Colima, Mexico earthquake of 22 January 2003, determined by joint inversion of teleseismic body-wave and near-source data. *Bull. Seismol. Soc. Am.* **94**, 1795–1807 (2004).
34. Wu, C. F., Lee, W. H. K. & Boore, D. M. Strong-motion data from the two Pingtung, Taiwan, earthquakes of 26 December 2006. *Terr. Atmos. Ocean. Sci.* **19**, 595–639 (2008).
35. Ampuero, J.-P. & Dahlen, F. A. Ambiguity of the moment tensor. *Bull. Seismol. Soc. Am.* **95**, 390–400 (2005).
36. Shimizu, K., Yagi, Y., Okuwaki, R. & Fukahata, Y. Development of an inversion method to extract information on fault geometry from teleseismic data. *Geophys. J. Int.* **220**, 1055–1065 (2020).
37. Kikuchi, M. & Kanamori, H. Inversion of complex body waves—III. *Bull. Seismol. Soc. Am.* **81**, 2335–2350 (1991).
38. Cundall, P. A. Numerical experiments on localization in frictional materials. *Ing. -Arch.* **59**, 148–159 (1989).
39. McIntosh, K. et al. Crustal-scale seismic profiles across Taiwan and the western Philippine Sea. *Tectonophysics* **401**, 23–54 (2005).
40. Li, Y. & Gurnis, M. Rapid shear zone weakening during subduction initiation. *Proc. Natl. Acad. Sci.* **121**, e2404939121 (2024).
41. Yu, S., Kuo, L., Punongbayan, R. S. & Ramos, E. G. GPS observation of crustal deformation in the Taiwan-Luzon Region. *Geophys. Res. Lett.* **26**, 923–926 (1999).
42. Tan, E. Subduction of transitional crust at the Manila Trench and its geophysical implications. *J. Asian Earth Sci.* **187**, 104100 (2020).
43. Li, C.-F. & Wang, J. Variations in Moho and Curie depths and heat flow in Eastern and Southeastern Asia. *Mar. Geophys. Res.* **37**, 1–20 (2016).
44. Sun, Y. et al. Three-dimensional thermal structure of East Asian continental lithosphere. *J. Geophys. Res. Solid Earth* **127**, e2021JB023432 (2022).
45. Tan, H., Gao, X., Wang, K., Gao, J. & He, J. Hidden roughness of subducting seafloor and implications for megathrust seismogenesis: Example From Northern Manila Trench. *Geophys. Res. Lett.* **49**, e2022GL100146 (2022).
46. Huang, T.-Y., Gung, Y., Kuo, B.-Y., Chiao, L.-Y. & Chen, Y.-N. Layered deformation in the Taiwan orogen. *Science* **349**, 720–723 (2015).
47. Ohara, K., Yagi, Y. & Okuwaki, R. Complex rupture evolution of the 2007 Martinique earthquake: a non-double-couple event in the Caribbean Sea. *Geophys. J. Int.* **236**, 1743–1752 (2024).
48. Abercrombie, R. E., Antolik, M. & Ekström, G. The June 2000 Mw 7.9 earthquakes south of Sumatra: Deformation in the India–Australia Plate. *J. Geophys. Res. Solid Earth* **108**, ESE 6-1 (2003).
49. Wu, J., Suppe, J., Lu, R. & Kanda, R. Philippine Sea and East Asian plate tectonics since 52 Ma constrained by new subducted slab reconstruction methods. *J. Geophys. Res. Solid Earth* **121**, 4670–4741 (2016).
50. Hu, J. & Angelier, J. Stress permutations: Three-dimensional distinct element analysis accounts for a common phenomenon in brittle tectonics. *J. Geophys. Res. Solid Earth* **109**, 2003JB002616 (2004).
51. Zhang, J., Sun, Z., Yang, H. & Zhang, F. A model of plate bending at the transition zone from subduction to collision in Northernmost Manila Trench. *Geophys. Res. Lett.* **49**, e2022GL100474 (2022).
52. Craig, T. J., Copley, A. & Jackson, J. A reassessment of outer-rise seismicity and its implications for the mechanics of oceanic lithosphere. *Geophys. J. Int.* **197**, 63–89 (2014).
53. Sandiford, D. & Craig, T. J. Plate bending earthquakes and the strength distribution of the lithosphere. *Geophys. J. Int.* **235**, 488–508 (2023).

54. Ye, L., Lay, T. & Kanamori, H. The 25 March 2020 M 7.5 Paramushir, northern Kuril Islands earthquake and major (M ≥ 7.0) near-trench intraplate compressional faulting. *Earth Planet. Sci. Lett.* **556**, 116728 (2021).
55. Kita, S., Okada, T., Hasegawa, A., Nakajima, J. & Matsuzawa, T. Existence of interplane earthquakes and neutral stress boundary between the upper and lower planes of the double seismic zone beneath Tohoku and Hokkaido, northeastern Japan. *Tectonophysics* **496**, 68–82 (2010).
56. Okuwaki, R. et al. Illuminating a contorted slab with a complex intraslab rupture evolution during the 2021 Mw 7.3 East Cape, New Zealand Earthquake. *Geophys. Res. Lett.* **48**, e2021GL095117 (2021).
57. Fletcher, J. M., Oskin, M. E. & Teran, O. J. The role of a keystone fault in triggering the complex El Mayor–Cucapah earthquake rupture. *Nat. Geosci.* **9**, 303–307 (2016).
58. Lay, T. et al. The 2009 Samoa–Tonga great earthquake triggered doublet. *Nature* **466**, 964–968 (2010).
59. Toussaint, G., Burov, E. & Jolivet, L. Continental plate collision: Unstable vs. stable slab dynamics. *Geology* **32**, 33 (2004).
60. Dal Zilio, L., van Dinther, Y., Gerya, T. V. & Pranger, C. C. Seismic behaviour of mountain belts controlled by plate convergence rate. *Earth Planet. Sci. Lett.* **482**, 81–92 (2018).
61. Burov, E. B. The upper crust is softer than dry quartzite. *Tectonophysics* **361**, 321–326 (2003).
62. Kay, R. W. & Kay, S. M. The nature of the lower continental crust: Inferences from geophysics, surface geology, and crustal xenoliths. *Rev. Geophys.* **19**, 271–297 (1981).
63. Kohlstedt, D. L., Evans, B. & Mackwell, S. J. Strength of the lithosphere: Constraints imposed by laboratory experiments. *J. Geophys. Res. Solid Earth* **100**, 17587–17602 (1995).
64. Mouthereau, F. & Petit, C. Rheology and strength of the Eurasian continental lithosphere in the foreland of the Taiwan collision belt: Constraints from seismicity, flexure, and structural styles. *J. Geophys. Res. Solid Earth* **108**, 2002JB002098 (2003).
65. Handy, M. R. & Brun, J.-P. Seismicity, structure and strength of the continental lithosphere. *Earth Planet. Sci. Lett.* **223**, 427–441 (2004).
66. Sandiford, D., Moresi, L. M., Sandiford, M., Farrington, R. & Yang, T. The Fingerprints of Flexure in Slab Seismicity. *Tectonics* **39**, e2019TC005894 (2020).
67. Chen, W.-P. et al. Moho, seismogenesis, and rheology of the lithosphere. *Tectonophysics* **609**, 491–503 (2013).
68. Molnar, P. The Brittle-plastic transition, earthquakes, temperatures, and strain rates. *J. Geophys. Res. Solid Earth* **125**, e2019JB019335 (2020).
69. Emmerson, B. & McKenzie, D. Thermal structure and seismicity of subducting lithosphere. *Phys. Earth Planet. Inter.* **163**, 191–208 (2007).
70. Ueda, T., Obata, M., Ozawa, K. & Shimizu, I. The Ductile-to-Brittle Transition Recorded in the Balmuccia Peridotite Body, Italy: Ambient Temperature for the Onset of Seismic Rupture in Mantle Rocks. *J. Geophys. Res. Solid Earth* **125**, e2019JB017385 (2020).
71. Lin, A. T. & Watts, A. B. Origin of the West Taiwan basin by orogenic loading and flexure of a rifted continental margin. *J. Geophys. Res. Solid Earth* **107**, ETG 2-1 (2002).
72. Ellis, S. & Wang, K. Lithospheric strength and stress revisited: Pruning the Christmas tree. *Earth Planet. Sci. Lett.* **595**, 117771 (2022).
73. Sloan, R. A. & Jackson, J. A. Upper-mantle earthquakes beneath the Arafura Sea and south Aru Trough: Implications for continental rheology. *J. Geophys. Res. Solid Earth* **117**, B05402 (2012).
74. De Nardis, R. et al. Lithospheric double shear zone unveiled by microseismicity in a region of slow deformation. *Sci. Rep.* **12**, 21066 (2022).
75. Schulte-Pelkum, V. et al. Mantle earthquakes in the Himalayan collision zone. *Geology* **47**, 815–819 (2019).
76. Wen, K.-L., Chang, Y.-W., Lin, C.-M., Chiang, H.-J. & Huang, M.-W. Damage and Ground Motion of the 26 December 2006 Pingtung Earthquakes, Taiwan. *Terr. Atmos. Ocean. Sci.* **19**, 641 (2008).
77. Guo, H., Lay, T. & Brodsky, E. E. Seismological indicators of geologically inferred fault maturity. *J. Geophys. Res. Solid Earth* **128**, e2023JB027096 (2023).
78. Chatterjee, A., Trugman, D. T., Hirth, G., Lee, J. & Tsai, V. C. High-frequency ground motions of earthquakes correlate with fault network complexity. *Geophys. Res. Lett.* **51**, e2024GL109418 (2024).
79. Cebry, S. & McLaskey, G. Heterogeneous high frequency seismic radiation from complex ruptures. *Seismica* **3**, (2024).
80. Yagi, Y. & Fukahata, Y. Introduction of uncertainty of Green's function into waveform inversion for seismic source processes. *Geophys. J. Int.* **186**, 711–720 (2011).
81. Akaike, H. Likelihood and the Bayes procedure. in *Selected Papers of Hirotugu Akaike* (eds. Parzen, E., Tanabe, K. & Kitagawa, G.) 309–332 (Springer New York, New York, NY, 1998). https://doi.org/10.1007/978-1-4612-1694-0_24.
82. Fukahata, Y., Yagi, Y. & Matsu'ura, M. Waveform inversion for seismic source processes using ABIC with two sorts of prior constraints: Comparison between proper and improper formulations. *Geophys. Res. Lett.* **30**, 2002GL016293 (2003).
83. Sato, D. S. K., Fukahata, Y. & Nozue, Y. Appropriate reduction of the posterior distribution in fully Bayesian inversions. *Geophys. J. Int.* **231**, 950–981 (2022).
84. Yabuki, T. & Matsu'ura, M. Geodetic data inversion using a Bayesian information criterion for spatial distribution of fault slip. *Geophys. J. Int.* **109**, 363–375 (1992).
85. Yamashita, S., Yagi, Y. & Okuwaki, R. Irregular rupture propagation and geometric fault complexities during the 2010 Mw 7.2 El Mayor-Cucapah earthquake. *Sci. Rep.* **12**, 4575 (2022).
86. Yamashita, S. et al. Potency density tensor inversion of complex body waveforms with time-adaptive smoothing constraint. *Geophys. J. Int.* **231**, 91–107 (2022).
87. Okuwaki, R. & Fan, W. Oblique Convergence Causes Both Thrust and Strike-Slip Ruptures During the 2021 M 7.2 Haiti Earthquake. *Geophys. Res. Lett.* **49**, e2021GL096373 (2022).
88. Shimizu, K., Yagi, Y., Okuwaki, R. & Fukahata, Y. Construction of fault geometry by finite-fault inversion of teleseismic data. *Geophys. J. Int.* **224**, 1003–1014 (2021).
89. Yagi, Y. et al. Barrier-Induced Rupture Front Disturbances during the 2023 Morocco Earthquake. *Seismol. Res. Lett.* **95**, 1591–1598 (2024).
90. Ohara, K. et al. Complex evolution of the 2016 Kaikoura earthquake revealed by teleseismic body waves. *Prog. Earth Planet. Sci.* **10**, 35 (2023).
91. Lavier, L. L., Buck, W. R. & Poliakov, A. N. B. Factors controlling normal fault offset in an ideal brittle layer. *J. Geophys. Res. Solid Earth* **105**, 23431–23442 (2000).
92. Poliakov, A. N. B., Cundall, P. A., Podladchikov, Y. Y. & Lyakhovsky, V. A. An Explicit Inertial Method for the Simulation of Viscoelastic Flow: An Evaluation of Elastic Effects on Diapiric Flow in Two- and Three-Layers Models. in *Flow and Creep in the Solar System: Observations, Modeling and Theory* (eds. Stone, D. B. & Runcorn, S. K.) 175–195 (Springer Netherlands, Dordrecht, 1993). https://doi.org/10.1007/978-94-015-8206-3_12.
93. Tan, E., Lavier, L. L., Van Avendonk, H. J. A. & Heuret, A. The role of frictional strength on plate coupling at the subduction interface. *Geochem. Geophys. Geosyst.* **13**, 2012GC004214 (2012).
94. Chen, Y. & Morgan, W. J. A nonlinear rheology model for mid-ocean ridge axis topography. *J. Geophys. Res. Solid Earth* **95**, 17583–17604 (1990).
95. Hayes, G. P. et al. Slab2, a comprehensive subduction zone geometry model. *Science* **362**, 58–61 (2018).
96. Wu, Y.-M. et al. On the use of explosion records for examining earthquake location uncertainty in Taiwan. *Terr. Atmos. Ocean. Sci.* **24**, 685 (2013).

Acknowledgements
We thank the two anonymous reviewers for their constructive comments that improved the manuscript and acknowledge the editor for their support throughout the review process. WLH thanks B.-S. Huang, J.-C. Hu, and S. Wei for valuable discussions. This work was supported by Taiwan's National Science and Technology Council (NSTC) Grant 114-2116-M-001-017 (WLH and ET) and Japan Society for the Promotion of Science (JSPS) Grant-in-Aid for Transformative Research Areas (A) "Science of Slow-to-Fast Earthquakes" 24H01020 (RO).

Author contributions
Conceptualization: W.L.H., E.T., R.O., Y.Y. Methodology: W.L.H., E.T., R.O., Y.Y..Investigation: W.L.H., E.T., R.O., Y.Y. Visualization: W.L.H. Supervision: E.T.. Writing—original draft: W.L.H.. Writing—review & editing: W.L.H., E.T., R.O., Y.Y.

Competing interests
The authors declare no competing interests.

Additional information
Supplementary information The online version contains supplementary material available at https://doi.org/10.1038/s43247-025-02719-x.

Correspondence and requests for materials should be addressed to Wan-Lin Hu or Ryo Okuwaki.

Peer review information *Communications Earth & Environment* thanks Tianhaozhe Sun and the other, anonymous, reviewer(s) for their contribution to the peer review of this work. Primary Handling Editors: Luca Dal Zilio, Joe Aslin, and Aliénor Lavergne. [A peer review file is available].